

# A Long-Range Electric Field Solver for Molecular Dynamics Based on Atomistic-to-Continuum Modeling

Jeremy A. Templeton,<sup>\*,†</sup> Reese E. Jones,<sup>‡</sup> Jonathan W. Lee,<sup>†,||</sup> Jonathan A. Zimmerman,<sup>‡</sup> and Bryan M. Wong<sup>§</sup>

<sup>†</sup>Thermal/Fluids Science and Engineering, <sup>‡</sup>Mechanics of Materials Department, and <sup>§</sup>Materials Chemistry Department, Sandia National Laboratories, Livermore, California 94551-0969, United States

**ABSTRACT:** Understanding charge transport processes at a molecular level is currently hindered by a lack of appropriate models for incorporating nonperiodic, anisotropic electric fields in molecular dynamics (MD) simulations. In this work, we develop a model for including electric fields in MD using an atomistic-to-continuum framework. This framework provides the mathematical and the algorithmic infrastructure to couple finite element (FE) representations of continuous data with atomic data. Our model represents the electric potential on a FE mesh satisfying a Poisson equation with source terms determined by the distribution of the atomic charges. Boundary conditions can be imposed naturally using the FE description of the potential, which then propagate to each atom through modified forces. The method is verified using simulations where analytical solutions are known or comparisons can be made to existing techniques. In addition, a calculation of a salt water solution in a silicon nanochannel is performed to demonstrate the method in a target scientific application in which ions are attracted to charged surfaces in the presence of electric fields and interfering media.

## 1. INTRODUCTION

The application of molecular dynamics (MD) simulations for understanding complex processes at the atomic scale has witnessed a radical improvement in the past three decades.<sup>1</sup> At present, however, most MD simulations are still performed in periodic domains due to the difficulty of accurately prescribing boundary conditions that break the spatial symmetries and enable many problems of scientific and technological interest to be examined. For example, simulating the electric double layer that forms at the interfaces of charged surfaces and ionic solutions is difficult to model with conventional techniques based on periodic boundaries in applications where the domain is anisotropic or the application of boundary conditions is required. The recent United States Department of Energy Basic Energy Sciences report<sup>2</sup> on research needs in electrical energy storage devices points to the inability to represent inhomogeneous electric fields within MD as one of the most important barriers to MD playing a role in modeling charge transport in batteries and supercapacitors. This statement is a direct consequence of the aforementioned difficulty in breaking spatial symmetries in MD simulations. By examining the current methods for incorporating long-range electric field effects in MD, the limitation can be better understood.

MD simulations achieve their computational efficiency by using a cutoff radius,  $r_c$ , such that any two distinct atoms  $\alpha$  and  $\beta$  only interact if the distance between them,  $r_{\alpha\beta}$ , is such that  $r_{\alpha\beta} < r_c$ . The forces that convey the interactions are determined by the potential energy of the system comprised of empirical functions dependent on interatomic distances. The functional form of most MD potentials is such that the decay rate with distance is fast, implying the cutoff radius approximation is appropriate. However, the electric potential between two charged particles only decays as  $r_{\alpha\beta}^{-1}$ , so possibly an infinite amount of energy will be artificially removed from the system if this interaction

is truncated. Because including an interaction between any two atoms requires both additional memory storage and increased computational time, directly simulating charged atoms is intractable for all but the smallest systems. Therefore, algorithms which can approximate the Coulombic interaction between particles have been developed to model charged systems while retaining the scalability and the efficiency of MD. Two common approaches for computing long-range electrical interactions are Ewald summations<sup>3</sup> and the particle–particle/particle–mesh (PPPM) method.<sup>4</sup> Other notable long-range interaction methods are the particle–mesh Ewald technique<sup>5</sup> (similar to the PPPM method), charge sheets,<sup>6</sup> and the fast multipole method<sup>7</sup> for long-range Coulombic forces and the Ewald method for long-range dispersion forces.<sup>8</sup>

Long-range methods for calculating electrical forces are often derived from the following decomposition of the electric potential due to point charges:

$$\begin{aligned} U = k \sum_{\alpha \in \mathcal{A}} \sum_{\beta \in \mathcal{A}} & \left( \frac{q^\alpha q^\beta}{r_{\alpha\beta}} \right) \\ & \beta \neq \alpha \\ = k \sum_{\alpha \in \mathcal{A}} \sum_{\beta \in \mathcal{A}} & \left( \frac{q^\alpha q^\beta}{r_{\alpha\beta}} - \int \int \frac{\rho^\alpha(\mathbf{r}) \rho^\beta(\mathbf{r}')}{|\mathbf{r} - \mathbf{r}'|} d\mathbf{r} d\mathbf{r}' \right) \\ & \beta \neq \alpha \\ + k \sum_{\alpha \in \mathcal{A}} \sum_{\beta \in \mathcal{A}} & \int \int \frac{\rho^\alpha(\mathbf{r}) \rho^\beta(\mathbf{r}')}{|\mathbf{r} - \mathbf{r}'|} d\mathbf{r} d\mathbf{r}' - k \sum_{\alpha \in \mathcal{A}} \int \int \frac{\rho^\alpha(\mathbf{r}) \rho^\alpha(\mathbf{r}')}{|\mathbf{r} - \mathbf{r}'|} d\mathbf{r} d\mathbf{r}' \end{aligned} \quad (1)$$

**Received:** December 19, 2010

**Published:** May 05, 2011

where continuous charge densities  $\rho^\alpha$  are introduced based on the idea that long-range forces are less sensitive to the location of the charges. In eq 1,  $U$  is the total electrostatic potential energy of the system as a function of all the atoms in the system, denoted by the set  $\mathcal{A}$  and indexed by  $\alpha$  and  $\beta$  (separated by distance  $r_{\alpha\beta}$ ) with each atom having a charge  $q^\alpha$ . Coulomb's constant is represented by  $k$ . The first term accounts for short-range interactions between particles, while the remaining terms describe the long-range effects of smooth charge distributions associated with each atom,  $\rho^\alpha$ . In both the PPPM and Ewald methods, the short-range sum is truncated to include only near neighbors, while  $\rho^\alpha$  is represented using a Gaussian distribution as a finite-width approximation to the Dirac  $\delta$  function (although this is not strictly required by the PPPM method). While the terms based on  $\rho^\alpha$  appear redundant, this form of the equation is amenable to separation between short- and long-ranged interactions based on a cutoff radius. In this mode, the first term accounts for the electrostatic interaction between two charges within the cutoff radius. It is corrected by the second term, which is needed when the charge density of every atom is used to compute the third term in eq 1 for the long-range interactions. Ewald sums analytically solve this equation using the Fourier space representation of the convolution of each  $\rho^\alpha$ . The PPPM method instead restricts  $\rho^\alpha$  to a grid and then computes its Fourier transform to quickly solve for the total electrostatic potential. Of the two, the PPPM approach is more widely used than the older Ewald sum, particularly for large systems.<sup>9</sup> It can be further accelerated by choosing "assignment functions" narrower than  $\rho^\alpha$  to interpolate the forces and correcting the potential solve with a modified Coulomb Green's function.<sup>4</sup>

Despite the differences in performance that drive the preference of one method over the other, both use analysis in Fourier space to solve eq 1 and thus are applicable for systems containing at least one periodic direction. Further, there is no mechanism within the methods to assign commonly needed, general boundary conditions associated with continuous potential fields. Methods to enable these types of simulations have been successfully developed for specialized geometries. For example, two-dimensional Ewald sums have been used in slab geometries.<sup>10–12</sup> An alternative is to use the full three-dimensional Ewald sums and extend the computational domain in the nonperiodic direction,<sup>13</sup> although the domain may need to be enlarged three to five times in extent, thus increasing the computational expense and introducing Gibbs artifacts.<sup>14</sup> These approaches have been used to simulate a variety of physically important systems. Examples include a silicon nanochannel with dissolved NaCl<sup>15</sup> (a correction term is used to account for the channel's dipole moment),<sup>16</sup> biological membranes,<sup>17,18</sup> and ions at liquid/gas interfaces for systems with a net charge.<sup>19</sup> In addition, a great deal of expertise using these methods has been developed in the research community, and they have been extensively compared against each other to determine the most appropriate long-range electric field model for a particular problem.<sup>9,20,21</sup>

While much work has been done to examine fully periodic and slab periodic systems, the authors are unaware of any general formulation applicable to systems without periodicity. The present work aims to provide such a framework by developing a new method for computing the electric field within an atomistic-to-continuum (AtC) framework. AtC methods involve coupling the discrete atomic dynamics in MD to spatially continuous processes represented by finite elements (FE). See

the review article of Miller and Tadmor<sup>22</sup> for a comparison of AtC approaches for mechanics simulations in which the FE represents continuous displacements and stresses. For this application, however, the FE will compute the long-range electric field, while the MD calculates the atomic motion. Shape functions associated with the elements enable projection of the atomic point charges to a continuous function spanned by the FE basis. In this way, the present AtC approach can be thought of as extending the PPPM method to a general basis set beyond harmonic functions. The next section describes the mathematical formulation required to apply AtC techniques to resolving electronic interactions of particles over distances longer than the cutoff radius of their Coulombic interactions. The algorithmic framework used in this work is based on multiscale AtC coupling<sup>23</sup> as implemented in the MD code LAMMPS (see ref 24 and <http://lammps.sandia.gov> for more details about LAMMPS). The theory section is followed by Section 3 which presents some example calculations to demonstrate the method's performance and applications. Finally, some conclusions are offered in Section 4.

## 2. MATHEMATICAL FORMULATION

**2.1. Mathematical Framework for Multiscale Modeling.** The multiscale modeling framework used in this work is based on approximate FE projections of MD data to restrict atomic quantities to a FE mesh and corresponding interpolation operators to compute FE quantities on atoms.<sup>23</sup> The FE method is founded on approximating arbitrary integrable functions with a subset of functions contained in a space  $\mathcal{W}$ . In the case of a continuous charge density field  $\rho(\mathbf{x})$  for  $\mathbf{x} \in \Omega \subset \mathbb{R}^3$ ,  $\rho$  is weakly equivalent to a function  $\hat{\rho}(\mathbf{x}) \in \mathcal{W}$  if

$$\int w \hat{\rho} \, dV = \int w \rho \, dV, \quad \forall w \in \mathcal{W} \quad (2)$$

Now assume that the space  $\mathcal{W}$  can be spanned by a finite number of basis functions, denoted shape functions, with the  $I$ th function written as  $N_I$ , where indices  $I$  are in the finite set  $\mathcal{F}$ . Then the approximate charge density field can be written as

$$\hat{\rho} = \sum_{I \in \mathcal{F}} N_I(\mathbf{x}) \rho_I, \quad \forall \mathbf{x} \in \Omega \quad (3)$$

where  $\rho_I$  is the nodal charge density associated with the  $I$ th shape function. In order to determine the nodal charge densities  $\rho_I$ , the function  $\rho$  is projected onto  $\mathcal{W}$  in the least-squares sense according to the Bubnov–Galerkin formulation:

$$\sum_{J \in \mathcal{F}} \rho_J \int_{\Omega} N_I N_J \, dV = \int_{\Omega} N_I \rho(\mathbf{x}) \, dV, \quad \forall I \in \mathcal{F} \quad (4)$$

In standard FE notation,  $\int_{\Omega} N_I N_J$  is the  $IJ$ th entry of the "mass matrix", while  $\int_{\Omega} N_I \rho(\mathbf{x}) \, dV$  is the inner product of the continuous function  $\rho$  and the  $I$ th FE basis function.

With this formulation, the set of equations, eqs 2–4, is strictly only appropriate for reducing the dimensionality of continuous functions, so it must be modified to account for the discrete nature of atomic quantities in MD. Typically, FE data take the form of nodal densities (i.e., charge density), while the atomic data are primitive variables (i.e., charge). These distinct quantities can be related by defining atomic densities using a small but finite associated volume,  $\Delta V_\rho^\alpha$  (to be determined later). In this work, it is assumed that the MD and FE domains exactly coincide.

Because continuous integration is not well-defined over the discrete atomic locations, the projection of a continuous function onto its FE representation is performed in this work by summation over the atomic charges  $q^\alpha$ :

$$\sum_{J \in \mathcal{F}} \rho_J \int_{\Omega} N_I N_J dV = \sum_{\alpha \in \mathcal{A}} N_I^\alpha \frac{q^\alpha}{\Delta V_\rho^\alpha} \Delta V^\alpha, \quad \forall I \in \mathcal{F} \quad (5)$$

using the approximation:

$$\rho(\mathbf{x}^\alpha) \equiv \rho^\alpha = \frac{q^\alpha}{\Delta V_\rho^\alpha} \quad (6)$$

following the ideas introduced by Wagner et al.<sup>23</sup>

In eq 5, two notions of associated atomic volume are present. The physically motivated  $\Delta V_\rho^\alpha$  is a measure of the space occupied by atom  $\alpha$  such that  $\rho^\alpha$  is an approximation of the true bulk density. In contrast,  $\Delta V^\alpha$  is an integration quadrature weight used to make the discrete sum approximate the continuous integral. While there is no requirement that these two volumes associated with atom  $\alpha$  be equal, equating the two atomic volumes, i.e.,  $\Delta V_\rho^\alpha = \Delta V^\alpha$ , will prove advantageous. This equality enables the fundamental relationship between a continuous density and its associated atomic quantity to be derived as

$$\sum_{J \in \mathcal{F}} \rho_J \int_{\Omega} N_I N_J dV = \sum_{\alpha \in \mathcal{A}} N_I^\alpha q^\alpha, \quad \forall I \in \mathcal{F} \quad (7)$$

The notation used in these equations and the remainder of this work is as follows. Indices in the set  $\mathcal{F}$  are denoted by subscript Roman letters, while superscript Greek letters denote atomic indices from the set  $\mathcal{A}$  enumerating the atoms in the system.  $N_I^\alpha$  then denotes the value of the shape function associated with node  $I$  at the position of atom  $\alpha$ , i.e.,  $N_I(\mathbf{x}^\alpha)$ . The variables  $\rho$  and  $q$  denote charge density and charge, respectively. In the sequel, all explicit set associations will be removed except where needed for clarity.

To verify the appropriateness of eq 7, it can be related to continuum models of fluid flow by differentiating it with respect to time. On the right-hand side, the result is

$$\frac{d}{dt} \sum_{\alpha} N_I^\alpha q^\alpha = \sum_{\alpha} q^\alpha \frac{d}{dt} N_I^\alpha = \sum_{\alpha} q^\alpha \nabla N_I^\alpha \cdot \mathbf{v}^\alpha \quad (8)$$

The time derivative of the left-hand side produces two terms:

$$\frac{d}{dt} \left[ \sum_J \rho_J \int_{\Omega} N_I N_J dV \right] = \sum_J \left[ \frac{d\rho_J}{dt} \int_{\Omega} (N_I N_J dV) + \rho_J \int_{\Omega} \frac{d}{dt} (N_I N_J dV) \right] \quad (9)$$

The term multiplying  $d\rho_J/dt$  is the standard FE mass matrix while

$$\int_{\Omega} \frac{d}{dt} (N_I N_J dV) = \frac{d}{dt} \left( \int_{\Omega} N_I N_J dV \right) = 0 \quad (10)$$

because the shape functions are fixed in the spatial domain and do not change with the movement of the atoms. To get eq 8 into the appropriate form, consider

$$\begin{aligned} \sum_{\alpha} q^\alpha \nabla N_I^\alpha \cdot \mathbf{v}^\alpha &= \sum_{\alpha} \nabla N_I^\alpha \cdot (\rho^\alpha \mathbf{v}^\alpha) \Delta V^\alpha \\ &\approx \int_{\Omega} \nabla N_I \cdot (\rho \mathbf{v}) dV \end{aligned}$$

The accuracy of the approximation of this equation is a function only of the approximate MD quadrature with weights  $\Delta V^\alpha$ .

The standard, continuous time evolution equation for density  $\rho$  is

$$\frac{d\rho}{dt} + \nabla \cdot (\rho \mathbf{v}) = 0 \quad (11)$$

which has the usual FE approximation:

$$\sum_J \frac{d\rho_J}{dt} \int_{\Omega} N_I N_J dV = - \int_{\Omega} N_I \nabla \cdot (\rho \mathbf{v}) dV \quad (12)$$

$$= \int_{\Omega} \nabla N_I \cdot (\rho \mathbf{v}) dV - \int_{\Gamma} N_I (\rho \mathbf{v}) \cdot \mathbf{n} dS \quad (13)$$

where  $\Gamma$  is the boundary of the set  $\Omega$ . Hence, if the atomic quadrature is exact and if there is no flux of atoms in or out of the system, then the standard FE approximation to the charge conservation equation is obtained which verifies the approach's consistency. The precision of the quadrature is related to the number of atoms in each element, so as the ratio of atoms per element becomes large, the correct continuous transport equation is recovered.

**2.2. Electric Field Model.** 2.2.1. *Long-Range Electric Field.* The emphasis of this work is on the formulation of an AtC electric field in which long-range interactions are computed on a FE mesh and communicated to the atoms, while short-range interactions are modeled directly by Coulombic interactions to maintain high fidelity. Each charged atom contributes to the electric potential, and because the potential is long-range, a direct restriction of the electric potential would be prohibitively costly, just as direct computation of the long-range Coulombic interactions is costly. Instead, the equation governing the electric potential will be solved on the FE mesh. The continuous equation governing the electric potential is

$$\nabla^2 \phi = -\frac{1}{\epsilon_0} \rho \quad (14)$$

with  $\epsilon_0$  being the dielectric constant.

It is now necessary to determine what FE equations the electric potential should satisfy. Standard FE practice is to multiply by the shape functions and integrate by parts to reduce the smoothness requirements on the solution, a procedure which produces:

$$\int_{\Omega} \nabla N_I \cdot \nabla \phi dV = \frac{1}{\epsilon_0} \int_{\Omega} N_I \rho dV - \int_{\Gamma} N_I \mathbf{E} \cdot \mathbf{n} dS \quad (15)$$

Here, the electric field is given by  $\mathbf{E} = -\nabla\phi$  and must be prescribed on boundaries with a free potential  $\phi$ . If the FE electric potential is approximated by an expansion in the shape functions:

$$\hat{\phi}(\mathbf{x}) = \sum_I N_I(\mathbf{x}) \phi_I \quad (16)$$

and the continuous charge density is approximated by the FE projection in eq 7, the FE equation for the potential is

$$\sum_J \phi_J \int_{\Omega} \nabla N_I \cdot \nabla N_J dV = \frac{1}{\epsilon_0} \sum_J \rho_J \int_{\Omega} N_I N_J dV - \int_{\Gamma} N_I \mathbf{E} \cdot \mathbf{n} dS \quad (17)$$

where we recognize the first matrix  $\int_{\Omega} \nabla N_I \cdot \nabla N_J dV$  as the usual "stiffness" matrix of FE and the second  $\int_{\Omega} N_I N_J dV$  as the "mass"

matrix. In contrast to the AtC projection, continuous integrals are retained because all quantities involved are continuous. This difference highlights the contrast between intrinsic (atomic-based) and extrinsic (non-atomic-based) fields.

**2.2.2. Atomic Electric Field.** The equations described in the previous section provide a straightforward definition for the electric force on an atom due to the FE electric potential:

$$\mathbf{f}_{e,FE}^\alpha = q^\alpha \mathbf{E} = -q^\alpha \nabla \hat{\phi}(\mathbf{x}^\alpha) \equiv -q^\alpha \sum_I \nabla N_I^\alpha \varphi_I \quad (18)$$

While this force could account for the entirety of the electrical interactions present in a system of interest, it would be impractical because the FE mesh resolution would have to be such that there were more elements than atoms to obtain a grid-converged solution. Alternately, all the Coulombic interactions could be explicitly incorporated according to

$$\mathbf{f}_{e,C}^\alpha = \sum_{\beta \in \mathcal{N}_\alpha} \frac{kq^\alpha q^\beta}{r_{\alpha\beta}^2} \mathbf{r}'_{\alpha\beta} \quad (19)$$

where  $\mathbf{r}'_{\alpha\beta}$  is the unit vector in the direction of  $\mathbf{r}_{\alpha\beta} = \mathbf{x}_\beta - \mathbf{x}_\alpha$ .

In order to effectively blend eqs 18 and 19 into a unified formalism, the FE electric field must be split into two parts:  $\hat{\phi} = \hat{\phi}^{la} + \hat{\phi}^{sa}$ . The first term,  $\hat{\phi}^{la}$ , represents the potential due to charges from all atoms outside of the cutoff radius,  $\mathcal{N}_\alpha \setminus \mathcal{N}_\omega$  and the imposed boundary conditions, i.e., the long-range interactions. It satisfies eq 17 with a modified nodal charge density  $\rho_j^{la}$  given by

$$\sum_J \rho_J^{la} \int_\Omega N_I N_J dV = \sum_{\beta \in \mathcal{N}_\alpha} N_I^\beta q^\beta \quad (20)$$

The second part of the decomposition, denoted by  $\hat{\phi}^{sa}$ , accounts for the short-range contributions to the potential due to charges from individual atoms within the cutoff radius of atom  $\alpha$ , i.e.,  $\beta \in \mathcal{N}_\alpha$ , where  $\mathcal{N}_\alpha$  is the set of neighbors of atom  $\alpha$  (including  $\alpha$  itself). It is computed by solving eq 17 with homogeneous boundary conditions and a nodal charge density  $\rho_j^{sa}$  defined with a modification of eq 17:

$$\sum_J \rho_J^{sa} \int_\Omega N_I N_J dV = \sum_{\beta \in \mathcal{N}_\alpha} N_I^\beta q^\beta \quad (21)$$

Note that the decomposition is different for each atom and hence the dependence of the superscript on  $\alpha$ .

While the equations discussed in the previous subsection describe the FE component of the electrical interaction, combining the Coulombic interactions with two components of the electric field decomposition will provide a mechanism to balance fidelity and cost of the method. Tractability implies that a finite cutoff distance is needed, as is standard in MD.<sup>3</sup> Outside of this cutoff, the only information regarding charge interactions between two particles is provided by the large-scale electric field. However, inside this cutoff radius the electrostatic force is most accurately described by Coulomb's law. Within this framework, the total electrostatic force on atom  $i$  is

$$\mathbf{f}_e^\alpha = \sum_{\beta \in \mathcal{N}_\alpha} \frac{kq^\alpha q^\beta}{r_{\alpha\beta}^2} \mathbf{r}'_{\alpha\beta} - q^\alpha \nabla \hat{\phi}^{la}(\mathbf{x}^\alpha) \quad (22)$$

The force has been decomposed into a Coulombic and FE long-range force. Recall the potential decomposition implies:

$$\nabla \hat{\phi}^{la}(\mathbf{x}^\alpha) = \nabla \hat{\phi}(\mathbf{x}^\alpha) - \nabla \hat{\phi}^{sa}(\mathbf{x}^\alpha) \quad (23)$$

Because the potential satisfies a linear equation, the short-range potential can be expressed as the sum of the electric potentials due to single atoms:

$$\hat{\phi}^{sa}(\mathbf{x}^\alpha) = \sum_{\beta \in \mathcal{N}_\alpha} \hat{\phi}^\beta \quad (24)$$

where the notation  $\hat{\phi}^\beta$  has been used to denote the potential arising from the charge associated with atom  $\beta$  only with homogeneous boundary conditions. By using eq 23 and eq 24, eq 22 can be rewritten as

$$\begin{aligned} \mathbf{f}_e^\alpha &= \sum_{\beta \in \mathcal{N}_\alpha} \frac{kq^\alpha q^\beta}{r_{\alpha\beta}^2} \mathbf{r}'_{\alpha\beta} - q^\alpha \left[ \nabla \hat{\phi}(\mathbf{x}^\alpha) - \sum_{\beta \in \mathcal{N}_\alpha} \nabla \hat{\phi}^\beta(\mathbf{x}^\alpha) \right] \\ &= \sum_{\beta \in \mathcal{N}_\alpha} \frac{kq^\alpha q^\beta}{r_{\alpha\beta}^2} \mathbf{r}'_{\alpha\beta} - q^\alpha \nabla \hat{\phi}(\mathbf{x}^\alpha) + q^\alpha \sum_{\beta \in \mathcal{N}_\alpha} \nabla \hat{\phi}^\beta(\mathbf{x}^\alpha) \end{aligned} \quad (25)$$

Equation 25 partitions the total electrostatic force between the exact Coulombic part at short ranges and a corrected FE accounting for the long-range energy and boundary conditions.

Accounting for a smoothly decreasing Coulombic energy between particles as occurs in many MD potentials (e.g., CHARMM)<sup>25</sup> is straightforward in this approach. Equation 22 is modified as follows:

$$\begin{aligned} \mathbf{f}_e^\alpha &= \sum_{\beta \in \mathcal{N}_\alpha} h(\mathbf{x}^\alpha, \mathbf{x}^\beta) \frac{kq^\alpha q^\beta}{r_{\alpha\beta}^2} \mathbf{r}'_{\alpha\beta} - q^\alpha \nabla \hat{\phi}^{la}(\mathbf{x}^\alpha) \\ &\quad - q^\alpha \sum_{\beta \in \mathcal{N}_\alpha} [1 - h(\mathbf{x}^\alpha, \mathbf{x}^\beta)] \nabla \hat{\phi}^\beta(\mathbf{x}^\alpha) \end{aligned}$$

where  $h$  is an arbitrary smoothing function. The resulting total force decomposition is

$$\mathbf{f}_e^\alpha = \sum_{\beta \in \mathcal{N}_\alpha} h(\mathbf{x}^\alpha, \mathbf{x}^\beta) \frac{kq^\alpha q^\beta}{r_{\alpha\beta}^2} \mathbf{r}'_{\alpha\beta} - q^\alpha \nabla \hat{\phi}(\mathbf{x}^\alpha) + q^\alpha \sum_{\beta \in \mathcal{N}_\alpha} h(\mathbf{x}^\alpha, \mathbf{x}^\beta) \nabla \hat{\phi}^\beta(\mathbf{x}^\alpha)$$

Given the expression for the total electrostatic force acting on atom  $\alpha$  in eq 25, the Coulombic interaction is computed from the MD, while the large-scale electric field is applied directly from the FE. It therefore remains to determine an effective manner in which to compute the contribution of the electric field at an atom strictly from its neighbors. Directly solving for the electric potential based on this set is a burdensome cost because it must be repeated over every atom and scales with the size of the FE mesh; a potentially significant burden for large three-dimensional grids. Instead, a method using Green's functions,  $G_K^I(\mathbf{x}) = \sum_K G_K^I(\mathbf{x}) G_K^I$ , computed on the FE mesh is preferable because it can be used to efficiently invert eq 17. The Green's function associated with the  $I^{\text{th}}$  node satisfies the system of equations:

$$\sum_K G_K^I \int_\Omega \nabla N_J \cdot \nabla N_K dV = \frac{1}{\epsilon_0} \delta_{IJ} \quad (26)$$

with  $\delta_{IJ}$  being the Kronecker  $\delta$ . Boundary conditions are taken to be homogeneous by definition in eq 26. The factor of  $1/\epsilon_0$ , while not necessary, is retained to facilitate later notation. The nodal variables  $G_J^I$  define the response of each mesh node,  $J$ ,

to an impulse at the  $I^{\text{th}}$  node, and can be recognized as scaled coefficients of the inverse stiffness matrix. A solution for the total potential at every node  $I$  can be written as

$$\varphi_I = \sum_J G_{IJ}^J f_J - \int_{\Gamma} N_I \mathbf{E} \cdot \mathbf{n} dS \quad (27)$$

where

$$f_J = \sum_K \rho_K \int_{\Omega} N_J N_K dV \quad (28)$$

Using this formulation, the potential due to only the neighbors is defined by two operations:

$$\sum_J \rho_J^\beta \int_{\Omega} N_I N_J dV = N_I^\beta q^\beta, \quad \forall \beta \in \mathcal{N}_\alpha \quad (29)$$

$$\phi_I^\beta = \sum_J \rho_J^\beta \left( \sum_K \int_{\Omega} N_J N_K dV \right) G_I^J \quad (30)$$

This framework allows the potential at atom  $\beta$  due to its neighbors to be easily evaluated. However, rather than solving eq 30 directly, substituting into it the right-hand side of eq 29 yields

$$\phi_I^\beta = \sum_{J \in \mathcal{F}^\beta} N_J^\beta q^\beta G_I^J \quad (31)$$

obviating the need to solve eq 29 for  $\rho_J^\beta$ . In fact, making a similar substitution in eq 17:

$$\sum_J \varphi_J \int_{\Omega} \nabla N_I \cdot \nabla N_J dV = \frac{1}{\epsilon_0} \sum_{\alpha} N_I^\alpha q^\alpha + \int_{\Gamma} N_I \mathbf{E} \cdot \mathbf{n} dS \quad (32)$$

means that  $\hat{\rho}$  itself need never be computed except as required for postprocessing, saving the computational cost of a matrix inversion. More importantly, eq 31 has been “localized” such that rather than have every node  $J$  included in the sum, instead a much smaller set, denoted by  $\mathcal{F}^\beta$ , is required. It is the set of shape function indices whose support includes atoms in the set  $\mathcal{N}_\beta$ . A graphical example is shown in Figure 1, and an algorithm for its determination is provided in algorithm 1 (see Chart 1). This algorithm guarantees that all nodes with shape functions corresponding to atom pairs that could be neighbors, if one of them is in the support of node  $I$ , are included but no others are. If the mesh size is bounded below, then the number of nodes retained in each sparsity pattern is bounded above and is independent of the total number of nodes in a mesh. This allows the short-range interactions to be correctly accounted for in an efficient manner.

The operation count for computing the short-range FE field using eqs 31 and 32 scales as  $O(n_{\mathcal{A}} n_{\mathcal{N}_\alpha})$ , where  $n_{\mathcal{A}}$  is the number of atoms, and  $n_{\mathcal{N}_\alpha}$  is the average number of neighbors per atom because  $n_{\mathcal{N}_\alpha}$  sums must be performed per atom. This is the same operation count as is needed to evaluate the long-range Coulombic interactions and naturally fits into the spatial decomposition mode of parallelism. However, the factor contained in the scaling itself depends on the number of FE nodes because each term in the sum involves a vector of data at each node. If a highly refined grid is used, the cost of evaluating the short-range FE electric forces will dominate the short-range Coulombic force computation.

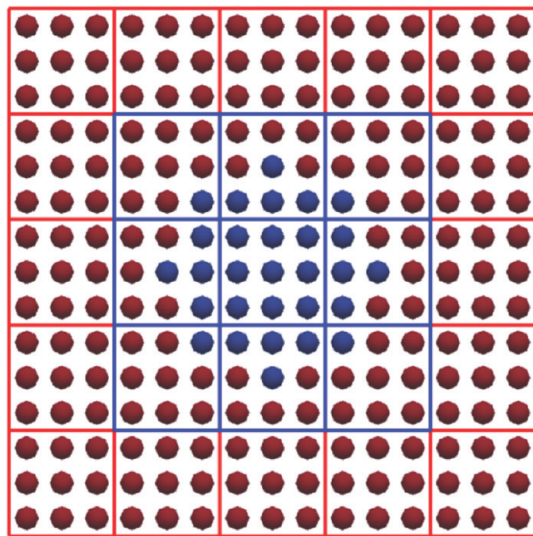


**Figure 1.** Schematic of the short-/long-range decomposition of the atoms within a cutoff radius and the nodes for which  $G_I^J$  is nonzero. Blue atoms are within the cutoff radius of the central atom, while red atoms are not. Similarly, the blue parts of the mesh denote the set of nodal Green's functions which must be retained for that atom, while the nodes in red part of the mesh will not contribute to the correction of the electric potential.

### Chart 1. Determination of Green's Function Sparsity Pattern for node $I$

#### Algorithm 1 Determination of Green's Function Sparsity Pattern for node $I$

```

1: set  $\mathcal{F}^\beta = \emptyset$ 
2: insert  $I$  into  $\mathcal{F}^\beta$ 
3: list NEIGHBORS = set of all nodes  $J \in \mathcal{F}$  such that  $\int_{\Omega} N_I N_J dV \neq 0$ 
4: insert all nodes in NEIGHBORS into  $\mathcal{F}^\beta$ 
5: enqueue nodes in NEIGHBORS into queue NEXT-NODES
6: while NEXT-NODES is not empty do
7:   pop NEXT-NODES to node  $J$ 
8:   list NEXT-NEIGHBORS = set of all nodes  $K \in \mathcal{F}$  such that  $K \notin \mathcal{F}^\beta$  and  $\int_{\Omega} N_J N_K dV \neq 0$ 
9:   insert all nodes in NEXT-NEIGHBORS into  $\mathcal{F}^\beta$ 
10:  if node  $J$  is within the cutoff radius of any node in NEIGHBORS then
11:    enqueue all nodes in NEXT-NEIGHBORS in NEXT-NODES
12:  end if
13: end while
14: return  $\mathcal{F}^\beta$ 

```

**2.3. Boundary Condition Models.** Imposing classical boundary conditions on MD systems presents a challenge because, at the scales of MD, boundary conditions are actually fluctuating quantities rather than fixed constraints. This section describes how some relevant types of boundary information can be applied within the present methodology. The first boundary conditions considered are Neumann conditions, which involve the normal derivatives that appear explicitly in eq 15. If the system is immersed in a strong and known electric field, setting  $\mathbf{E}$  at the boundaries to this quantity will impose the correct conditions. It can also be based on known currents because these are proportional to the electric field strength. If far-field data indicate there is no overall electric field or current,  $\mathbf{E}$  should be set to zero because that is correct on average. Accounting for the fluctuations in the boundary conditions as a result of the unsteadiness of the physics at the nanoscale is beyond the scope of this work.

The next case of interest is a charged infinite surface, which will occur in an MD calculation if one or two dimensions

parallel to the surface are periodic. Because an infinite surface carries infinite charge, a potential cannot be assigned to this surface. Rather, a bulk electric field should be applied perpendicular to the surface with strength based on the desired surface charge density. At the surface, the potential is set to zero so that the total electric potential is the superposition of two potentials arising from different sets of charge: (1) the charge that generates the bulk electric field and (2) the charged particles represented in the MD.

In addition to the surface charge, special considerations must be given for periodic boundaries. Within the current implementation, the potential is not computed in Fourier space and therefore cannot be determined to a global constant. Instead, a single (arbitrary) node is fixed to an arbitrary value, although other methods are possible (e.g., setting a global constraint on the average potential). A prerequisite for this approach is the net charge within the simulation box is zero, otherwise the spatially varying component of the potential due to point charges cannot be periodic. Further complications arise from the Green's function equation, eq 26. The Green's function of interest in this case is nonperiodic and infinite because the short-range charges should affect only interacting pairs rather than the infinite number of interactions of an atom with all the periodic images of its neighbors. Overcoming this challenge is possible, for example, the infinite Green's function can be approximated on a larger mesh or the analytic Green's function projected onto the existing basis. However, this approach will be deferred to future work. Instead the PPPM method is used to account for the electric forces in those directions, while the AtC approach only applies forces in the nonperiodic directions even though the electric potential is three-dimensional. A small error is introduced using this approach because the nonperiodic component will have a slight overcorrection due to the presence of its periodic images.

A final case of interest is the inclusion of a finite, fixed potential surface. For the purpose of developing appropriate models of such a surface in this work, a fixed potential surface is defined as a surface with a prescribed charge distribution such that the desired potential is the self-induced value everywhere on the surface. In contrast, a surface with a fixed charge will have a varying potential due to the presence of external charge sources, such as point charges. In large systems, it is reasonable to assume that an external voltage will maintain a potential roughly constant in time, but at the small time and length scales present in MD, this is an approximation. The surface charge would also depend on the electronic properties of the surface. For example, the surface charge in a conductor will vary to maintain the absence of an electric field inside the conducting body, while other surfaces would require a more complex relationship between surface charge and voltage. These effects are not included in the surface charge model that follows but are somewhat mitigated by the inclusion of short-range interactions with the wall.

Consider a fixed charged on a finite surface specified on a set of FE faces that must not be periodic in any direction. Because the faces are finite, a constant surface charge density will not maintain a constant potential. The potential due to a continuous charge  $\sigma(x)$  on a surface can be determined by

$$V(x) = \int_S \frac{k\sigma(s)}{\|x - s\|} ds \quad (33)$$

The FE projection for the voltage is

$$\begin{aligned} \sum_{J \in \mathcal{S}} V_J \int_S N_I N_J dS &= \int_S N_I V(s) dS \\ &= \int_S N_I \left( \int_{S'} \frac{k\sigma(s')}{\|s - s'\|} dS' \right) dS, \quad \forall I \in \mathcal{S} \end{aligned} \quad (34)$$

where  $\mathcal{S}$  is the set of FE nodes belonging to surface  $S$ . The integral on the right-hand side of eq 34 can be evaluated using standard FE face quadrature. As an aside, if the charge distribution is also defined by a FE expansion, then eq 34 becomes

$$\sum_{J \in \mathcal{S}} V_J \int_S N_I N_J dS = \sum_{J \in \mathcal{S}} \sigma_J \int_S N_I \left( \int_{S'} \frac{kN_J}{\|s - s'\|} dS' \right) dS, \quad \forall I \in \mathcal{S} \quad (35)$$

Equation 35 defines a linear relationship between the nodal potential on a surface and its associated nodal charge. The nodal charge for a fixed potential can be determined by solving eq 35 for  $\sigma_J$  while setting  $V_J$  to be fixed.

Within the multiscale framework for the electric potential, the surface charge will play a similar role to the atomic charges in that they both induce a long-range potential and provide short-range interactions. To consider these types of interactions, we further expand eq 25 by accounting for the surface charge in the electric potential:

$$\begin{aligned} f_e^\alpha &= \sum_{\beta \in \mathcal{N}_\alpha} \frac{kq^\alpha q^\beta}{r_{\alpha\beta}^2} r'_{\alpha\beta} + q^\alpha \sum_I \sigma_I \int_{S \cap B(x^\alpha, r_c)} \frac{kN_I}{\|x^\alpha - s\|^2} r'_{\alpha\beta} dS - q^\alpha \nabla \hat{\phi}^\alpha \\ &\quad + q^\alpha \sum_{\beta \in \mathcal{N}_\alpha} \nabla \hat{\phi}^\beta(x^\alpha) + q^\alpha \int_{S \cap B(x^\alpha, r_c)} \nabla \hat{\phi}_s^\alpha dS \end{aligned} \quad (36)$$

The first integral accounts for the exact short-range force exerted by the surface charge, while the second integral is a correction removing the effect of the surface charge through the FE potential on atom  $\alpha$ . Both integrals can be evaluated directly using FE quadrature, although other quadrature schemes are possible (e.g., based on atoms contained in those faces). The potential induced by the surface charge can be determined by computing Green's functions for each of the quadrature points by first solving eq 35 for the induced surface potential of a unit charge and then solving the electric potential equation treating the surface as a fixed potential boundary. This results in additional Green's functions for each quadrature point in the surface.

In general, these Green's functions are highly nonlocal because charge at any point on a surface induces a nonzero potential everywhere on the surface, as shown in eq 35. However, the resulting short-range interactions can still be localized by truncating the Green's functions to only those nodes within a cutoff radius of the surface, in exactly the same manner as was done for the point charges. The surface Green's functions can also be computed and stored during a precomputation phase. This method is a low-storage, low-cost approach that accounts for accurate short- and long-range interactions between charged MD atoms and prescribed surface data. An important point to note is that for any quadrature scheme used to evaluate the surface integrals in eq 36, each quadrature point will require its own Green's function.

**2.4. Implementation Details.** The methods described above were implemented in LAMMPS within an existing AtC framework.

This framework generates a FE mesh overlaying a region of atoms and computes piecewise linear shape function values and derivatives at FE quadrature points and atomic locations. A preprocessing step first computes the list of neighboring nodes for each node based on the force cutoff radius according to algorithm 1 (see Chart 1). Then the stiffness matrix is set up for the electric potential, eq 32, and used to compute each Green's function according to eq 26. Green's functions are then truncated and stored in sparse vectors based on the nodal neighbor lists. At the same time, fixed potential boundary values are determined by eq 34. Then the Green's function for each surface quadrature point used to evaluate eq 34 is calculated by solving eq 32. The bulk of the work of this method occurs immediately after the LAMMPS force calculation step, which is between the two steps in the standard Verlet time integration scheme.<sup>1</sup> At each time step, the shape functions  $N_I^\alpha$  used in the projection operation eq 7 must be updated to the new positions of the atoms.

After the shape function-related quantities are updated, the charges can be restricted using eq 7 with row-sum lumping to form the right-hand side for the FE electric potential, eq 32, enabling its calculation using the precomputed stiffness matrix. Neumann conditions are applied by adjusting the right-hand side during the solve, while Dirichlet conditions are satisfied by a penalty method. This method weights the diagonal entry of all fixed nodes with a value  $10^4$  greater than the maximum diagonal value in the left-hand side matrix. Correspondingly, the right-hand side is modified by adding the same penalty factor multiplying the desired potential value. It should be noted that other matrix solution schemes would perform adequately in this application.

LAMMPS adds in the Coulombic interaction before the present method is executed, so only the last two terms in eq 25 need to be accounted for. The first, accounting for the total FE electric field, is added to all atoms. Afterward, the truncated FE potential associated with each atom is computed using the Green's functions multiplied by the restricted atomic charges. This preprocessing step allows the neighbor FE potentials for each atom to be quickly calculated by summing over the FE potential contribution of all its neighbors. The potential is then corrected to result in the appropriate electric force at each atom using eq 25.

Charged surfaces are implemented in an approximate manner. In a preprocessing step, consistent with a form of row-sum lumping approximation of eq 34, the potential is determined from a fixed charge by

$$V_I = \sum_{y \in \mathcal{Q}} \frac{k\sigma(y)}{|x_I - y|} w(x_I, y) \quad (37)$$

where  $\mathcal{Q}$  denotes the location of the Gauss quadrature points on the face, and  $w$  is the associated quadrature weight. This approach ensures the denominator is always nonzero. To evaluate the short-range interactions, the nodes are used as effective charge locations with charge set to the shape-function weighted integral of the surface charge:

$$\eta_I = \int_{\Gamma} N_I \sigma(x) dS \quad (38)$$

with the integral evaluated using the same Gaussian quadrature as eq 37. Note that  $\eta_I$  is the effective charge associated with node  $I$  and not a nodal value of a finite element representation of  $\hat{\sigma}$ .

When computing the short-range surface interactions and corrections in eq 36, only nodes within the cutoff radius of each atom are considered, and then their Green's functions are used to

remove the FE potential. As a simplifying approximation, face-specific Green's functions are not computed for the charge at each quadrature point that contributes to the charge at node  $I$  in eq 38. Instead, only their contributions to the potential at node  $I$  are considered, which allows the same Green's functions, as those used in eq 31, to be reused. The net effect of all these approximations is that low-order integration is used to evaluate the first integral in eq 36, while the correction from the second integral does not take into account all the long-range impact of local charge on the fixed potential boundary condition applied in eq 32.

Improvements to the surface charge fidelity can be made by improving the order of integration over the surface within the cutoff radius and more accurately estimating the impact of charge associated with quadrature points on the electric potential. A final improvement in performance can be realized by maintaining neighbor lists at each surface quadrature point to avoid the search over all atoms to determine those near a wall. (Walls are currently implemented in LAMMPS with this more expensive approach as well.) These improvements in the implementation of charged surfaces as well as more general models for other types of surfaces and periodic boundary corrections for eq 25 are deferred for future work.

### 3. COMPUTATIONAL RESULTS

**3.1. Comparison with Analytic Results.** To verify the basic correctness and implementation of the method, a simple stack of atoms was set up with fully periodic conditions along the span ( $y, z$ ). Periodic conditions on the atomic forces were also used along the length of the stack ( $x$ ) to maintain the equilibrium structure. An FCC lattice structure with spacing 4.08 Å, resulting in 144 atoms, was used to develop a test case amenable to analytical solution. Around this lattice a FE mesh was constructed to represent the continuous charge distributions and electric field. While the elements have nonzero volume, periodicity in the  $y$  and  $z$  directions effectively makes the elements one-dimensional with length 2.04 Å. However the FE mesh is not periodic in the  $x$  direction so fixed potential and electric field boundary conditions can be applied. The overall structure is shown in Figure 2a.

The electric field in this case was driven by both boundary conditions and internal charges. Each atom was given a unit charge (equivalent of a proton) such that the system's charge density was uniform at  $5.89 \times 10^{-2}$  unit charges per Å<sup>3</sup>. The FE potential was fixed to zero at the left end. At the right end, either an insulating or a fixed electric field condition was used. The known boundary conditions and charge densities allow the analytic solution to Poisson's equation to be determined. All the calculations in Section 3 used a 10 Å cutoff radius. As shown in Figure 2, in both cases the analytic solution is recovered by the method. This case tests the Poisson solver and projection operations. The results verify their implementation and demonstrate that the overall mathematical formulation of the problem is reasonable given the behavior of the FE system.

**3.2. Comparison with Existing Methods: PPPM and Ewald Sums.** Providing a quantitative comparison of the present method with existing approaches for including long-range electrostatic forces in MD is an important aspect of verifying the technique. These are primarily PPPM and Ewald sums as described in Section 1. Since these methods are only appropriate for periodic systems, a fully periodic FCC lattice system is created

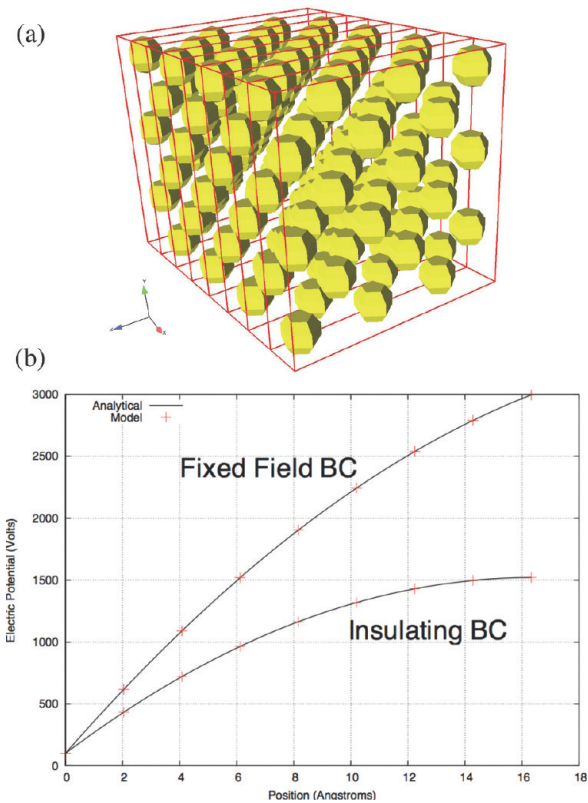


**Figure 2.** Basic verification test case: (a) shows the problem set up, while (b) presents the results for different boundary conditions.

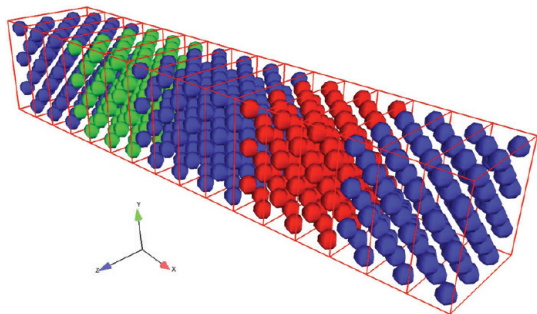


**Figure 3.** Schematic of the PPPM and Ewald comparison case with the present method. Red atoms are positively charged, green atoms are negatively charged, and blue atoms are neutral.

with dimensions  $65.28 \times 12.24 \times 12.24 \text{ \AA}^3$  and lattice spacing of  $4.08 \text{ \AA}$ , composed of 576 atoms. The atoms are uncharged except for a group with a positive unit charge and a group with a negative unit charge, as shown in Figure 3 (which also shows the finest FE mesh). Initial computations were performed with the short-range Coulombic force disabled so that the only forces acting on the atoms are the long-range forces generated by the method. Hence the issues with periodicity affecting the short-range correction discussed in Section 2.3 do not affect this calculation. As shown in Table 1, the proposed AtC method produces forces similar to the other methods. In each case the force acting on the negatively charged atoms is presented because the net force was zero for all methods. To see how this is related to the FE fields, Figure 4 shows the FE charge density and the electric potential

**Table 1. Comparison of the Force Computed by the Long-Range Electric Field<sup>a</sup>**

force ( $\text{g ps}/\text{\AA}^2 \text{ mol}$ )	method/mesh
$8.49533 \times 10^6$	PPPM
$8.49543 \times 10^6$	Ewald sums
$4.71971 \times 10^6$	$8 \times 1 \times 1$ elements
$8.49547 \times 10^6$	$16 \times 1 \times 1$ elements
$8.49547 \times 10^6$	$32 \times 1 \times 1$ elements
$8.49547 \times 10^6$	$32 \times 2 \times 2$ elements
$8.49547 \times 10^6$	$32 \times 4 \times 4$ elements

<sup>a</sup> The present method, with entries denoted by the mesh size, is shown along with existing approaches. Execution times were also compared using software profiling tools. The  $16 \times 1 \times 1$  element AtC computation was slightly more expensive than the PPPM method and considerably cheaper than the Ewald summations. As the grid is refined the cost increases, with the  $32 \times 1 \times 1$  and  $32 \times 2 \times 2$  element meshes bracketing the cost of the Ewald solution. Note the AtC electric field solver has not been optimized, while the existing methods in LAMMPS and their associated fast fourier transforms are highly optimized.

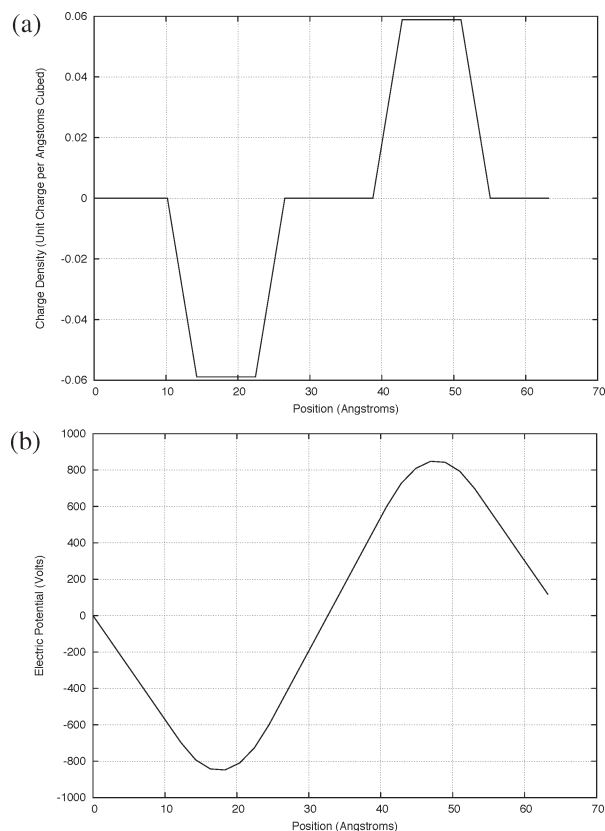


**Figure 4.** Finite element fields from the finest mesh used to compare against the PPPM method and Ewald Sums. (a) Charge density and (b) electric potential using this charge density as a source.

variables. The charge density is simply the approximate projection of the atomic state and enters into the right-hand side of the equation governing the electric potential. On the coarsest mesh, inadequate resolution exists to accurately solve the gradients needed in this equation, resulting in significant error in the solution.

This test demonstrates the correctness of the theory and implementation regarding the prolongation of the long-range

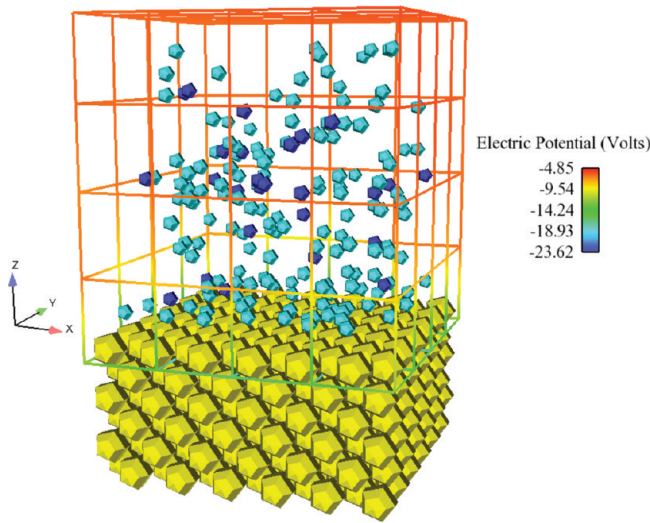


**Figure 5.** Schematic of the argon/gold configuration. Gold atoms are yellow, neutral argon atoms are light blue, and positively charged argon atoms are dark blue. Particles are kept in the box using 9-3 LJ walls at each unbounded side of the mesh, which is colored using the electric potential.

force from the FE to the atoms, including the use of FE shape functions to take derivatives of the electric potential. It further demonstrates that the method has accuracy comparable to existing methods, even though the finest FE grid had only 256 elements, while the automatically generated PPPM method required a grid of  $2.592 \times 10^6$  ( $320 \times 90 \times 90$ ) Fourier collocation points to achieve a relative error of  $10^{-4}$ . This is the only case considered in this work in which a fully periodic system could be used because dynamics were not evaluated, and therefore the short-range FE correction was not needed (recall the current correction scheme is not designed for handling periodic directions). However, to use the FE method the node corresponding to the origin was fixed to have zero potential so the Poisson equation would be well-posed.

**3.3. Comparison with Full Anisotropic Solution.** For the purposes of comparing the proposed method to its alternatives, there is one other way to incorporate long-range electrical interactions between charged particles in MD: “brute force” calculation of the electric field using a finite MD simulation with a Coulombic cutoff distance greater than the maximum possible atomic separation. For most simulations, the cost of building the neighbor lists and computing the interatomic electrical interactions would prevent application of this method. Furthermore, it is inappropriate for periodic systems because an infinite cutoff radius would be required. While such limitations render such an approach impractical for computations of scientific interest, a small model problem has been developed that serves as a surrogate for an electric double layer. This problem also enables investigation of some of the complex boundary conditions that can be applied. At the wall, a fixed surface charge condition will be used, which introduces some error by transforming into a fixed potential boundary condition at long distances. Also, Neumann conditions will be used to prescribe the remaining boundary conditions on the electric field, but as will be shown, this is an approximation because there is no way of knowing what the normal component of the electric field should be.

The model system built to examine this case consists of an FCC gold lattice with spacing  $4.08 \text{ \AA}$  over a horizontal span of  $22.44 \times 22.44 \text{ \AA}^2$ . The lattice is not periodic in any direction, and these atoms are held fixed. They serve as an effective force field on a system of liquid argon on top of this structure to a height of  $22.44 \text{ \AA}$ . Dimensions of the box were selected to be the maximum size such that the neighbor lists could fit in the available memory and still be long enough for atoms at opposite ends of the box to be neighbors. The fluid used was argon, which was equilibrated at 300 K for 50 ps with a time step of 0.5 fs using the Nosé–Hoover thermostat.<sup>26</sup> A schematic of the system, including the FE mesh, is shown after the equilibration step in Figure 5. Upon creation, certain argon atoms were randomly chosen to have a positive unit charge so that during equilibration they tend to separate. Argon atoms were confined by 9-3 Lennard-Jones (LJ) walls along the five sides without gold, with the energy given by

$$E = \varepsilon_{93} \left[ \frac{2}{15} \left( \frac{\sigma_{93}}{r} \right)^9 - \left( \frac{\sigma_{93}}{r} \right)^3 \right], \quad r < r_c \quad (39)$$

with  $\varepsilon_{93} = 0.0195 \text{ eV}$  and  $\sigma_{93} = 3.45 \text{ \AA}$ . Interatomic forces were modeled using LJ interactions, i.e.:

$$E_i = 4\varepsilon_i \left[ \left( \frac{\sigma_i}{r} \right)^{12} - \left( \frac{\sigma_i}{r} \right)^6 \right], \quad r < r_c \quad (40)$$

Parameters for LJ interactions are the energy depth of the well  $\varepsilon$ , the length scale  $\sigma$ , and the cutoff radius  $r_c$ . Gold–gold interactions use  $\varepsilon = 0.724 \text{ eV}$  and  $\sigma = 2.598 \text{ \AA}$ , while the argon–argon model has  $\varepsilon = 0.010 \text{ eV}$  and  $\sigma = 3.405 \text{ \AA}$ . A uniform cutoff radius of  $13.0 \text{ \AA}$  was used for the interatomic LJ interactions, while  $r_c = 10 \text{ \AA}$  for the wall and short-range electrical interactions when using the AtC method. Cross-species interactions were parameterized by mixing the potential parameters according to the rules  $\varepsilon_{ij} = (\varepsilon_i \varepsilon_j)^{1/2}$  and  $\sigma_{ij} = (\sigma_i + \sigma_j)/2$ .

After equilibration, the top layer of gold atoms is negatively charged so that it can be exactly screened by the ions. This configuration is run to a statistical steady state using either only Coulombic interactions with a long cutoff distance of  $40 \text{ \AA}$  or the present method with a much more modest cutoff of  $13 \text{ \AA}$ . As already mentioned, exactly resolving all long Coulombic interactions was the limiting factor in choosing this geometry. The FE mesh was created to cover the liquid using  $7 \times 7 \times 7$  uniform elements of size approximately  $48 \text{ \AA}^3$ . When using the AtC method the gold atom charge was removed and accounted for by use of a fixed charge boundary and its corresponding spatially varying surface potential, as described in the previous section. Fixing the gold atoms was chosen in order to remove surface deformation phenomena from the problem, with a consequence being that the wall acts as a cold surface. Zero normal electric field (Neumann) boundary conditions were used on all other sides, which serves as a rough approximation to the true electric field’s behavior when the long cutoff is used.

This case illustrates the difficulty in exactly translating continuous boundary conditions to an atomistic setting. An insulating condition is only appropriate in the limit of an infinitely small screening layer such that the electric field is zero outside of the domain of interest. This limit is violated even in the steady state of this solution and is clearly incorrect during the transient. Further, the charged surface is treated as a fixed potential surface by the FE electric potential, when in reality the potential varies based on the distribution of the atoms. In a true conductor, for

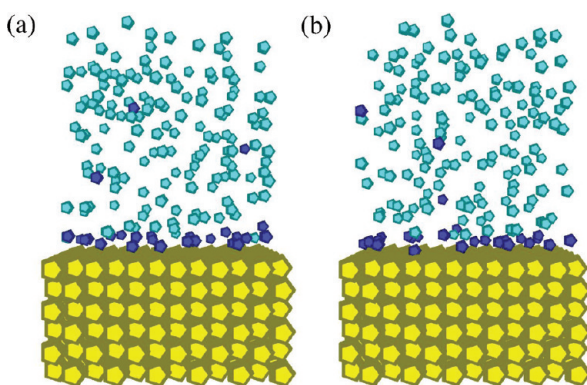


**Figure 6.** Comparison of the final MD state from: (a) the direct calculation and (b) the AtC method. See Figure 5 for the color legend.

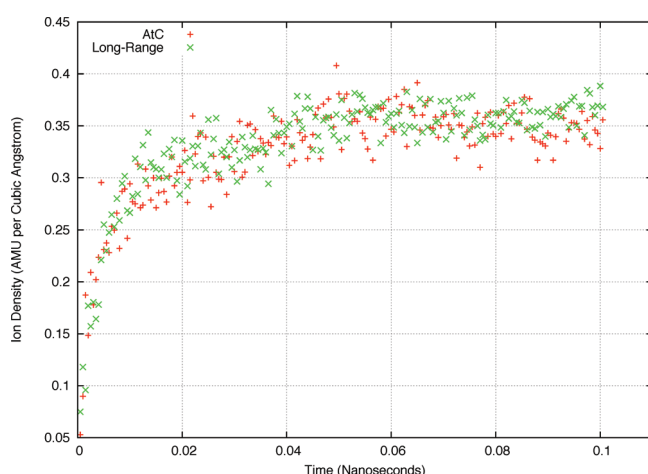


**Figure 7.** Time history of the plane-averaged charged argon density at the FE node adjacent to the gold.

example, the potential and surface charge would change to make the electric field in the conductor zero. Derivations in this work have focused on developing the general framework for the long-range potential in terms of solving an appropriately sourced Poisson equation in conjunction with the standard fixed potential and insulating boundary conditions encountered in electrostatics. While a few enhancements have been made to approximate surfaces with a fixed charge, boundary models to better account for the physics are left for future work.

Despite the inconsistency noted above, the exact MD solution can be compared against the MD solution using the long-range FE electric field. However, it is sufficient to obtain reasonable quantitative comparisons between the two solutions since the bulk of the potential drop occurs both very near and perpendicular to the gold surface. In both cases, 24 charged atoms lie in an immobile layer near the wall, while three remain mobile above this layer (based on the particles' trajectories, one of the free atoms is partially screened). By congregating near the wall, these atoms screen the electric field so it drastically reduces in magnitude away from the wall. The dynamics of these atoms indicate they are highly attracted to the charged wall as they experience only a vibrational motion after their adsorption, however there is a limit to how densely they can be packed.

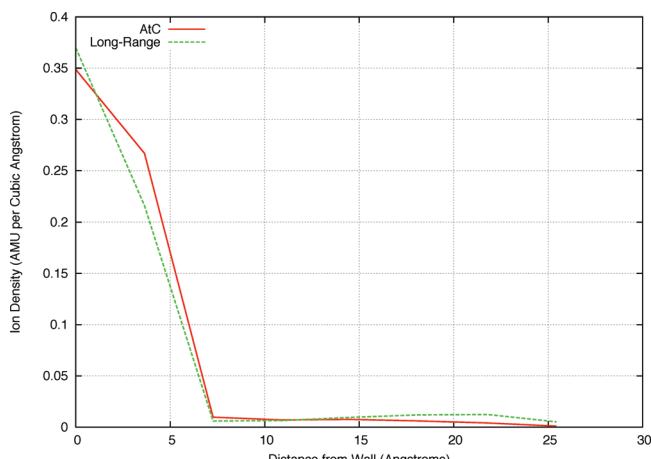


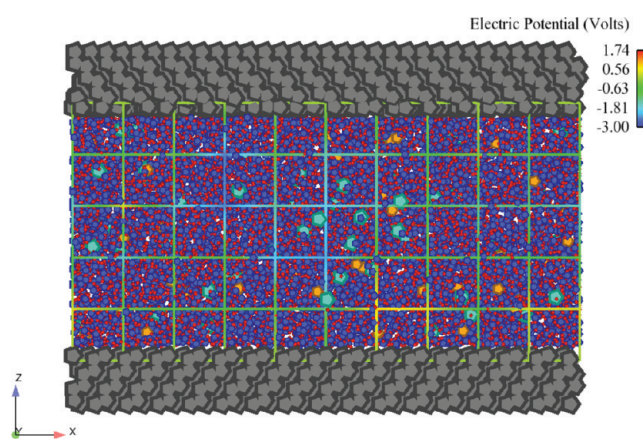
**Figure 8.** Time-averaged nodal charged argon densities at the steady state.

The AtC method can also be used to extract comparable quantitative data from the simulation. After the gold is charged, an initial transient occurs during which the free charged argon atoms form the immobile screening layer on the wall. It can be visualized by examining the time history of the nodal charged argon density adjacent to the wall. The atomic configuration is visualized in Figure 6, while Figure 7 shows this density averaged over the first node of the FE calculation (a similar mesh was set up over the long-range cutoff geometry for postprocessing only, exactly as in Figure 5). Both cases have nearly identical rise times with the density in the long-range case being slightly higher than the AtC case. Given how the data is partitioned in FE, this indicates the location of the layer is slightly closer to the wall when the long-range Coulombic cutoff is used. To determine precisely the difference in the height of the layers, the simulation is run for an additional nanosecond with the density data averaged over nodes at the same vertical distance from the gold. As shown in Figure 8, despite the approximate nature of the insulating FE boundary conditions and the low-order quadrature used to implement the charged surface, good agreement is obtained with the exact solution when using this method in both quantitative and qualitative senses.

**3.4. Electrolyte Flow in a Silicon Nanochannel.** In this case, flow in a nanofluidic device is considered. A full analysis of this configuration is beyond the scope of this work, but the case illustrates how to perform these types of technologically relevant simulations. Silicon crystals form walls at the top and the bottom of a region of salt water, which is free to flow in the wall-parallel directions. Periodic conditions are used to allow this flow, while the channel walls break the symmetry. Table 2 gives the potential type, coefficients, and source for each pair of interactions considered in the simulations. References refer to relevant simulations that used these parameters in similar physical situations, except for the Stillinger–Weber (SW), where the originating reference for this potential is provided. All short-range charged interactions were modeled using Coulombic interactions with a sharp cutoff at 10 Å. Water is modeled using the TIP3<sup>28</sup> set of pairwise LJ coefficients and with charges on the oxygen of −0.830 and the hydrogen of 0.415 in terms of fractions of a proton charge. For the Morse potential the parameters are the energy  $D_0$ , inverse length scale

**Table 2. Interaction Potential, Potential Coefficients, And References for Pairwise Interactions in the Silicon Nano-channel Simulation**

atom 1	atom 2	potential	coefficients	source
O	O	LJ	$\epsilon = 0.006740, \sigma = 3.1650, r_c = 10$	28
O	Na	LJ	$\epsilon = 0.005348, \sigma = 3.24085, r_c = 10$	15
O	Cl	LJ	$\epsilon = 0.005348, \sigma = 3.77535, r_c = 10$	15
O	Si	Morse	$D_0 = 0.0668, \alpha = 1.3, r_0 = 3.7, r_c = 9$	15
Na	Na	LJ	$\epsilon = 0.004336, \sigma = 3.331, r_c = 10$	15
Na	Cl	LJ	$\epsilon = 0.004336, \sigma = 3.8655, r_c = 10$	15
Na	Si	LJ	$\epsilon = 0.0056043, \sigma = 2.9645, r_c = 10$	15
Cl	Cl	LJ	$\epsilon = 0.004336, \sigma = 4.4, r_c = 10$	15
Cl	Si	LJ	$\epsilon = 0.056043, \sigma = 3.499, r_c = 10$	15
Si	Si	SW	see <sup>27</sup>	27

**Figure 9.** Schematic of the silicon nanochannel simulation. Water is modeled using hydrogen atoms (red) bonded to oxygen atoms (blue). Other atoms are sodium ions (orange), chlorine ions (light blue), and silicon (gray). The FE mesh is overlaid and colored by the electric potential.

$\alpha$ , equilibrium distance  $r_0$ , and cutoff radius  $r_c$ :

$$E = D_0[e^{-2\alpha(r - r_0)} - 2e^{-\alpha(r - r_0)}], \quad r < r_c \quad (41)$$

The units used are Å for length and eV for energy. Note that hydrogen atoms only interact with other atoms electrically. In general, interactions were chosen to match the model of Qiao and Aluru<sup>15</sup> in the case of the silicon nanochannel.

Figure 9 illustrates the computational geometry. The silicon planes are initialized in a similar manner to the gold in Section 3.3 except for the periodic boundaries in the transverse direction. The silicon is arranged in a diamond lattice with the [111] face toward the water, and then the arrangement is adjusted to minimize the potential energy to account for the exposed  $\pm z$  faces. A box of water containing 16 sodium and 16 chlorine ions dissolved in 1819 water molecules is initialized for 1 ns, using a time step of 0.5 fs, in a fixed region using the Nosé–Hoover thermostat to maintain a fixed temperature of 300 K and 9-3 LJ walls to contain the fluid in the wall-normal directions. After equilibration, the water (without the LJ walls) is inserted between the silicon planes and allowed to readjust for 1 ns. During this phase, the water was integrated using Newtonian dynamics, while the Nosé–Hoover thermostat was applied to

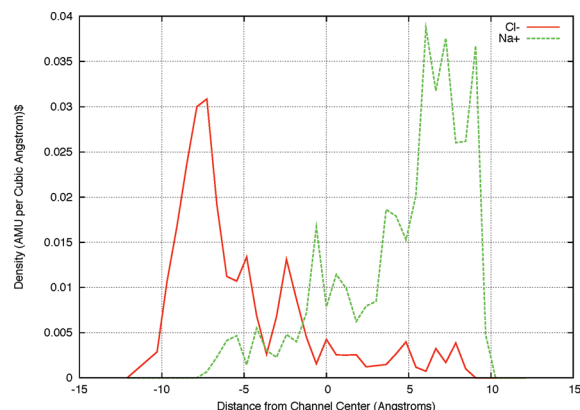
the silicon so it could thermally regulate the salt water. After the entire system comes into equilibrium, electric fields of strength  $-1 \text{ V/nm}$  were applied in the  $x$  (wall-parallel) and  $z$  (wall-normal) directions. With these fields in place, ions of opposite charge are forced to flow along the channel in opposite directions as well as aggregate to opposite sides of the channel, resulting in shear flow in the channel. Statistics were captured after running for 0.1 ns using the method of Zimmerman et al.<sup>29</sup>

A similar case was originally considered by Qiao and Aluru using a different methodology to account for the ionic electric field by applying a wall-normal correction to the Ewald summations used to compute the long-range electrostatic interactions in the periodic directions.<sup>16</sup> In addition, the potential drop was applied by fictitiously charging the silicon atoms.

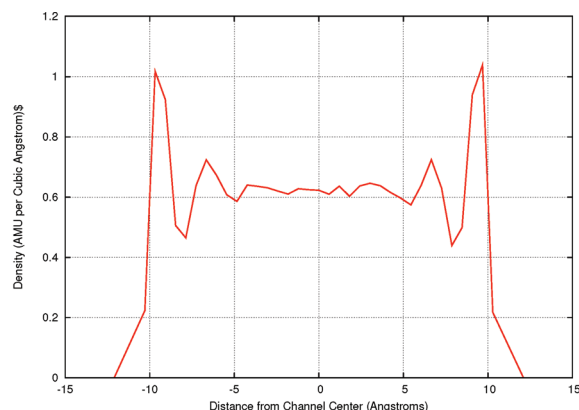
The present method instead decomposes the electric potential into three components and uses the most appropriate method for each. To account for the applied voltage drop in the wall-normal direction, a fixed electric field was used requiring minimal additional computation. Similarly, the wall-parallel flow was driven by a fixed electric field. Electrical interactions induced by water and ions in the wall-parallel directions were handled using the PPPM method in LAMMPS in a slab mode (and explicitly removing wall-normal forces). Motivating the use of PPPM for this component of the field is the fact that using the Fourier basis is more efficient than a general FE basis, whereas the AtC method's purpose is to account for inhomogeneous directions with Dirichlet and Neumann boundary conditions. The Green's functions used to correct the short-range interactions by the AtC method are nontrivial to implement correctly for periodic boundaries because if they account for the periodicity they will remove too much force, as noted in Section 2.3. Specifically, the long-range forces from periodic images of nearby atoms will be canceled. Note the short-range electrostatic interactions are handled using the standard Coulombic formulation implemented directly in LAMMPS.

As previously noted, the PPPM approach requires approximations in the wall-normal direction, which can be avoided by using the AtC method to compute the wall-normal electric potential. In order to have the correct total potential when each component is summed, fixed (zero) potential boundary conditions are used at the layer of silicon atoms adjacent to the salt water. Use of these boundary conditions also mitigates the numerical errors in the wall-normal direction of the periodic Green's functions. Grid spacing of the AtC FE mesh is chosen to be half the cutoff radius to minimize the impact of errors from the electric field solve on the atomic forces. In general, the grid spacing should be less than the cutoff radius because of the numerical errors associated with approximating the delta functions due to the point charges in the source term. However, within the present formulation, if a fixed cutoff radius is used, then the total electrical interactions will converge with mesh refinement. A fully three-dimensional grid is used for the AtC solve so that spatial variations in the electric field are accounted for in the wall-normal electric forces. Periodic boundary conditions are applied in the wall-parallel directions to the AtC FE solution to generate an accurate electric potential. This approach of decomposing the total potential therefore enables each method to be used to greatest effect.

The results of this calculation demonstrate the appropriateness of using the AtC electric potential in directions in which spatial symmetries are broken. In this case, an electric double layer forms on each surface mitigated by the wall-normal electric forces. As in the case of Qiao and Aluru, insufficient charge is

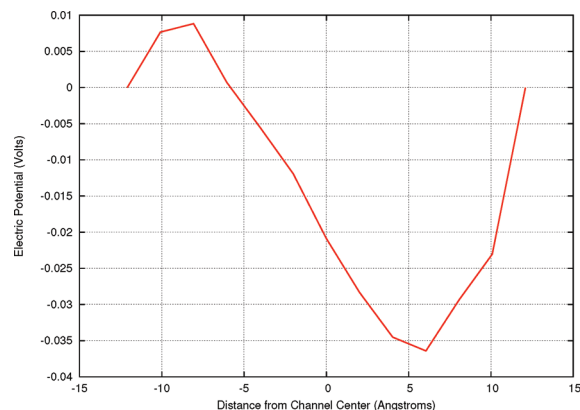


(a) Ion Distribution in the Nanochannel

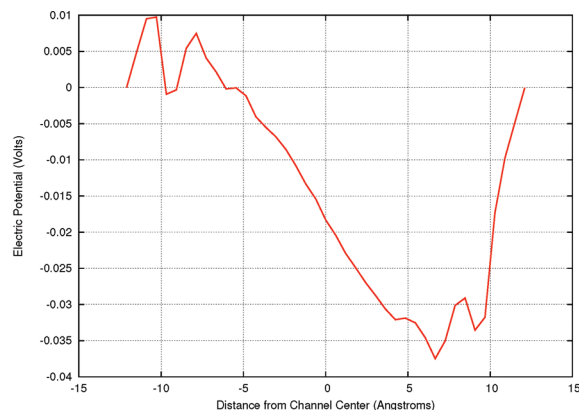


(b) Water Molecule Distribution in the Nanochannel

Figure 10. Plane-averaged wall-normal density profiles of the species present in the nanochannel: (a) charged ions and (b) water molecules.



(a) Nominal Mesh Electric Potential



(b) Refined Mesh Electric Potential

Figure 11. Plane-averaged wall-normal electric potential induced by ions in the nanochannel: (a) nominal mesh and (b) refined mesh.

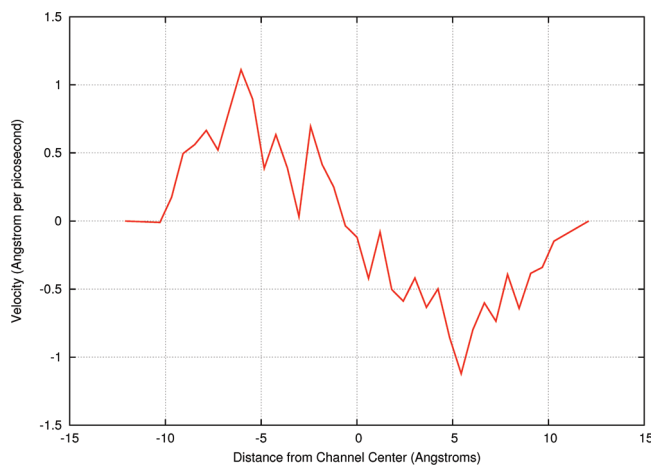


Figure 12. Plane-averaged wall-normal velocity profile of the water molecules.

included in the solution to fully screen the applied electric field. Some ions form an adsorbed layer adjacent to the wall, while others remain in solution but preferentially distributed based the electric field, as shown in Figure 10. Both the ions and water

demonstrate layering effects based on the electric field and nanoscale dimensions of the channel. Figure 11 illustrates how the electric potential induced by the ions reflects this structure with near wall extrema. The field is much smoother than the ionic distributions because the element size is greater than the layering size. Therefore short-range electrical interactions account for the ionic layering, while the long-range effects determine the interaction between the species segregated on opposite walls. Calculating this potential with sufficient fidelity to accurately capture the long-range interactions is critical. To demonstrate an appropriate mesh spacing exists, a further run was performed using an eight-fold mesh refinement in the wall-normal direction. The resulting potential, provided in Figure 11b, now has multiple near-wall extrema due to the layering. However, this structure is not needed for the long-range interactions, and the observation that the overall potential drop and the field structure are unchanged verifies the appropriateness of the original mesh. Finally, the resulting velocity profile is presented in Figure 12, confirming the flow is slower near the channel center as it is primarily driven by the ions in the double layers near the walls. In a technological application, this would be the relevant quantity determining device performance.

## 4. CONCLUSIONS AND FUTURE WORK

This work describes a method to apply consistent anisotropic electric fields, including prescribed boundary conditions, to molecular dynamics simulations. By using AtC coupling, the electric potential can be solved on a FE mesh using source terms arising from the atomistic charge distribution. The approach is a significant improvement over current schemes for incorporating long-range electrical interactions, which are restricted to periodic domains. By breaking this symmetry, the AtC electric field enables simulations of more technologically relevant configurations with applied electric fields or potential surfaces.

The AtC coupling methodology in this work can be thought of as a generalization of previous methods, such as PPPM, to a wider set of basis functions for representing the electric potential. By choosing appropriate functions from this set, a framework has been developed that does not rely upon periodic boundary conditions to compute long-range electrical interactions. Three core numerical techniques comprise the method. The first is restriction of atomic charge information to a continuous density fields represented on a FE mesh, similar to kernel estimation. Next, the electric potential is solved on the FE mesh using a Poisson equation with appropriate sources based on electrostatics. Finally, the electric forces due to this potential are computed on a per-atom basis and corrected based on resolved short-range interactions. The FE potential solve allows for standard fixed potential and fixed field boundary conditions. In addition, approximate boundary conditions for charged surfaces were also presented. Periodic boundaries are currently handled through combining this approach with existing long-range electric field methods.

To demonstrate the correctness of this method, four example simulations were performed. To verify the restriction of atomic information and the Poisson solution, including Dirichlet and Neumann boundary conditions, a simple block of charged atoms was considered. Excellent agreement between the resulting electric potentials with analytic solutions was obtained. Next, the method was compared with the PPPM and Ewald sum techniques implemented in LAMMPS using a charge neutral bar with blocks of opposite charge separated by more than the Coulombic interaction cutoff distance. All three methods computed the forces between the charged blocks to four significant digits, showing the accuracy of the atomic projection step. The case also demonstrated reasonable mesh size guidelines. A final verification problem examined a small box of fluid argon atoms, some charged, some not, in the presence of a charged surface. Direct MD computations were possible by retaining a very long cutoff radius for the Coulombic interactions. Comparison with the proposed method was possible by using approximate boundary conditions at the charged surface as well as zero-field conditions on the other sides of the box. Despite these approximations, good agreement was demonstrated between the method for both the transient development of the layer of charged argon near the surface and for the steady-state ion density profiles.

While the previous simulations compared the proposed method to existing analytical and numerical solutions, they did not examine the technique in one of its intended applications. Therefore, flow in a silicon nanochannel was modeled using the AtC method to compute shear flow in a NaCl solution between oppositely charged plates. This case demonstrates the steps that must be taken to perform these simulations by incrementally building and equilibrating the various components, such as silicon and water,

followed by applying separate models for the isotropic and anisotropic components of the electric field. As expected, ions congregated near oppositely charged walls, while a parallel electric field accelerated the ions, causing a shear flow to develop. These results show that information relevant to both scientific understanding and technological applications can be obtained using this formulation.

As demonstrated by the various simulations, this technique enables MD to be used to examine a new class of problems in which spatial symmetries are not present, making periodic boundary conditions inappropriate. The ability to prescribe boundary conditions means that interactions with the environment can be included in an approximate manner. However, defining physically appropriate boundary conditions for molecular systems is challenging and depends on the type of environment. Future work will enhance the method by developing appropriate boundary conditions for other types of physics, e.g., conducting and insulating surfaces. Error analysis, based on the FE mesh spacing, and the Coulombic cutoff radius will also be considered to automate the mesh generation process. Even without these features, the present method still represents an important improvement in MD capabilities by enabling long-range electric field effects to be incorporated in complex geometries with a generalized set of boundary conditions.

## ■ AUTHOR INFORMATION

### Corresponding Author

\*E-mail: jatempl@sandia.gov.

### Present Addresses

<sup>†</sup>Rice University, Department of Mechanical Engineering and Materials Science, Houston, Texas, United States.

## ■ ACKNOWLEDGMENT

Sandia National Laboratories is a multiprogram laboratory managed and operated by Sandia Corporation, a wholly owned subsidiary of Lockheed Martin Corporation, for the U.S. Department of Energy's National Nuclear Security Administration under contract DE-AC04-94AL85000. Funding for this work was provided by the Laboratory Directed Research and Development program at Sandia National Laboratories, and its support is gratefully acknowledged. The authors appreciate P. Crozier, G. Wagner, and S. James for providing helpful comments on a draft of this manuscript. The sparse vector software used in this work was implemented by J. Oswald.

## ■ REFERENCES

- (1) Frenkel, D.; Smit, B. *Understanding Molecular Simulation: From algorithms to applications*; Academic Press: San Diego, CA, 2002.
- (2) Goodenough, J.; et al. *Basic Research Needs for Electrical Energy Storage*; Technical Report; Office of Science, U.S. Department of Energy: Washington, DC, 2007.
- (3) Allen, M.; Tildesley, D. *Computer Simulation of Liquids*; Clarendon Press: Oxford, U.K., 1987.
- (4) Hockney, R.; Eastwood, J. *Computer Simulation using Particles*; Taylor & Francis Group: Bristol, PA, 1988.
- (5) Darden, T.; York, D.; Pedersen, L. *J. Chem. Phys.* **1993**, *98*, 10089–10092.
- (6) Torrie, G.; Valleau *J. Chem. Phys. Lett.* **1979**, *65*, 343.
- (7) Greengard, L.; Rokhlin, V. *J. Comput. Phys.* **1987**, *73*, 325–348.
- (8) in 't Veld, P. J.; Ismail, A. E.; Grest, G. S. *J. Chem. Phys.* **2007**, *127*, 144711.

- (9) Pollock, E.; Glosli, J. *Comput. Phys. Commun.* **1996**, *95*, 93–110.  
(10) Parry, D. E. *Surf. Sci.* **1975**, *49*, 433–440.  
(11) Heyes, D.; Barber, M.; Clarke, J. H. R. *J. Chem. Soc., Faraday Trans. 2* **1977**, *73*, 1485–1496.  
(12) de Leeuw, S. W.; Perram, J. W. *Mol. Phys.* **1979**, *37*, 1313–1322.  
(13) Shelley, J.; Patey, G.; Berard, D.; Torrie, G. *J. Chem. Phys.* **1997**, *107*, 2122–2141.  
(14) Spohr, E. *J. Chem. Phys.* **1997**, *107*, 6342–6348.  
(15) Qiao, R.; Aluru, N. *J. Chem. Phys.* **2003**, *118*, 4692–4701.  
(16) Yeh, I.-C.; Berkowitz, M. *J. Chem. Phys.* **1999**, *111*, 3155.  
(17) Yang, Y.; Henderson, D.; Crozier, P.; Rowley, R.; Busath, D. *J. Chem. Phys.* **1983**, *79*, 926–935.  
(18) Sachs, J.; Crozier, P.; Woolf, T. *J. Chem. Phys.* **2004**, *121*, 10847–10851.  
(19) Ballenegger, V.; Arnold, A.; Cerdá, J. *J. Chem. Phys.* **1983**, *79*, 926–935.  
(20) Crozier, P.; Rowley, R.; Spohr, E.; Henderson, D. *J. Chem. Phys.* **2000**, *112*, 9253–9257.  
(21) Patra, M.; Hyvonen, M.; Falck, E.; Sabouri-Ghomí, M.; Vattulainen, I.; Karttunen, M. *Comput. Phys. Commun.* **2007**, *176*, 14–22.  
(22) Miller, R.; Tadmor, E. *Model. Simul. Mater. Sci. Eng.* **2009**, *17*, 053001.  
(23) Wagner, G.; Jones, R.; Templeton, J.; Parks, M. *Comput. Meth. Appl. Mech. Eng.* **2008**, *197*, 3351–3365.  
(24) Plimpton, S. *J. Comput. Phys.* **1995**, *117*, 1–19.  
(25) MacKerell, A.; *J. Phys. Chem. B* **1998**, *102*, 3586–3616.  
(26) Hoover, W. *Phys. Rev. A* **1985**, *31*, 1695–1697.  
(27) Stillinger, F.; Weber, T. *Phys. Rev. B* **1985**, *31*, 5262–5271.  
(28) Jorgensen, W.; Chandrasekhar, J.; Madura, J.; Impey, R.; Klein, M. *J. Chem. Phys.* **1983**, *79*, 926–935.  
(29) Zimmerman, J.; Webb, E.; Hoyt, J.; Jones, R.; Klein, P.; Bammann, D. *Model. Simul. Mater. Sci. Eng.* **2004**, *12*, S319–S332.